ORIGINAL PAPER

Deformation localisation in stretched liquid crystal elastomers

Rabin Poudel[1] · Yasemin Şengül[1] · L. Angela Mihai[1]

© The Author(s) 2024

Abstract

We model within the framework of finite elasticity two inherent instabilities observed in liquid crystal elastomers under uniaxial tension. First is necking, which occurs when a material sample suddenly elongates more in a small region where it appears narrower than the rest of the sample. Second is shear striping, which forms when the in-plane director rotates gradually to realign and become parallel with the applied force. These phenomena are due to the liquid crystal molecules rotating freely under mechanical loads. To capture necking, we assume that the uniaxial order parameter increases with tensile stretch, as reported experimentally during polydomain-monodomain transition. To account for shear striping, we maintain the uniaxial order parameter fixed, as suggested by experiments. Our finite element simulations capture well these phenomena. As necking in liquid crystal elastomers has not been satisfactorily modelled before, our theoretical and numerical findings related to this effect can be of wide interest. Shear striping has been well studied, yet our computed examples also show how optimal stripe width increases with the nematic penetration depth measuring the competition between the Frank elasticity of liquid crystals and polymer elasticity. Although known theoretically, this result has not been confirmed numerically by previous nonlinear elastic models.

Keywords Nematic elastomers · Mathematical models · Large-strain deformation · Necking · Shear striping · Finite elements

1 Introduction

Liquid crystal elastomers (LCEs) are formed from cross-linked polymeric chains with embedded liquid crystal (LC) molecules [49]. Due to this special architecture, they display both self-organisation under external stimuli, such as heating or illumination, and large reversible deformations under mechanical loads. In modern laboratories, LCEs are being prepared through various techniques. Typically, polydomain samples are obtained where the material contains multiple subdomains, with a different nematic alignment. The unit vector for the localised direction of uniaxial nematic alignment is termed the *director*. Monodomain LCEs can subsequently be achieved by applying electric or magnetic fields, or deforming the material mechanically to induce a desired nematic orientation.

There has been a long-standing interest in the multi-physics characteristics of nematic elastomers and incorporating them in muscle-like actuators and other advanced technologies [8, 22, 43, 50]. However, many fundamental questions concerning these material remain open and require further theoretical investigation.

✉ L. Angela Mihai
  MihaiLA@cardiff.ac.uk

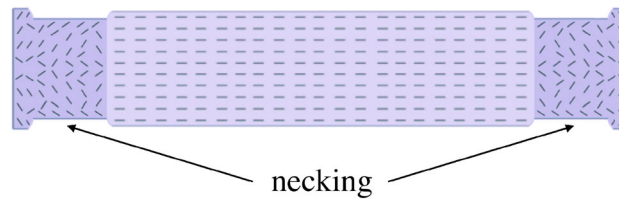1   School of Mathematics, Cardiff University, Cardiff, UK

Fig. 1 Schematics of nematic LCE developing necking under large stretch causing the initially disordered LC molecules to rotate until they align with the applied force in the horizontal direction. Darker colour at the ends signifies opacity in the physical sample where the LC molecules are randomly oriented, while the lighter colour in the middle corresponds to the physical sample being translucent where the LC molecules are uniformly aligned

Generally, under mechanical loads, the nematic director tends to rotate in order to align with the largest principal stretch [31, 38]. This rotation is not always uniform and can generate some interesting macroscopic effects. For example, when subject to a large tensile force, some LCEs exhibit localised necking [5, 6]. This phenomenon occurs when there is a critical extension ratio, such that the force required to extend the material beyond this critical value changes from increasing to decreasing. In this case, the homogeneous deformation becomes unstable, and the material sample suddenly elongates more in a small region than in the rest of the sample. Locally, the material appears much narrower than before the critical stretch was reached, as illustrated schematically in Fig. 1. Experimental evidence of LCE necking has been reported in [20, 21, 27]. Also, in [20], since necking could not be captured by the neoclassical LCE model based on the neo-Hookean strain-energy function for rubber, it was suggested that a viscoelastic model would be required instead. A finite element modelling of instabilities in viscoelastic nematic elastomers, including necking, is presented in [4]. However, within the theoretical framework of elasticity, a satisfactory mathematical model for LCE necking is still to be achieved.

Certain stretch deformations of LCEs also result in a pattern of parallel stripe subdomains where equal and opposite shear deformations occur in neighbouring stripes [18, 23]. The theoretical explanation for this phenomenon, which is depicted schematically in Fig. 2, is that the energy depending isotropically on the macroscopic deformation through the relative strain of the microstructure is minimised by a state of many homogeneously deformed parts. This is known as *soft* or *semi-soft elasticity*, since it is usually accompanied by a much slower increase in the required stress compared to prior and subsequent deformed states [3]. Shear stripes formation in elongated nematic LCEs [13, 21, 23, 24, 40, 41, 46, 52] has been extensively analysed theoretically [1–3, 7, 10, 11, 15–17, 23, 31, 32, 34, 35, 37] or simulated numerically [30, 45], and it is therefore well understood.

In this paper, first we introduce a class of theoretical models for LCEs (Section 2), then show how necking can be captured under uniaxial tensile load (Section 3). We also revisit the modelling of LCE shear striping under uniaxial tension, providing an analytical solution and estimating stripe periodicity [48] (Section 4). These models are further implemented in a finite element code to simulate the respective effects (Section 5). Necking in LCEs has not been satisfactorily modelled before, so both our theoretical and numerical findings related to this effect can be of wide interest. While shear striping has been well studied, our numerical examples also show how optimal stripe width increases with the nematic penetration depth measuring the competition between the Frank elasticity of LCs and polymer elasticity. This result, although known theoretically, has not been captured numerically by previous nonlinear elastic models.
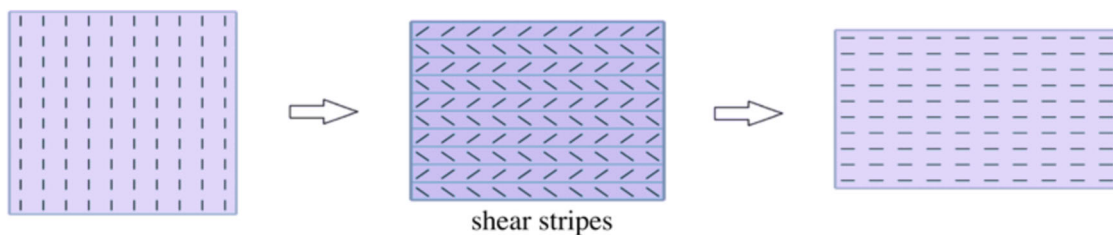

Fig. 2 Schematics of nematic LCE developing shear stripes under large stretch causing the initial director in the vertical direction to rotate until it aligns with the applied force in the horizontal direction. Darker colour in the middle figure signifies opacity in the physical sample where the shear stripes form, while lighter colour in the left- and right-hand figures corresponds to the physical sample being translucent where the LC molecules are uniformly aligned

2 Model function

To describe an incompressible nematic LCE, we consider the following strain-energy function [17]

$$W^{(lce)} = \frac{\mu^{(1)}}{2}\left(\lambda_1^2 + \lambda_2^2 + \lambda_3^2 - 3\right) + \frac{\mu^{(2)}}{2}\left(\alpha_1^2 + \alpha_2^2 + \alpha_3^2 - 3\right),$$ (1)

where $\mu = \mu^{(1)} + \mu^{(2)} > 0$ is the shear modulus at infinitesimal strain, with $\mu^{(1)}, \mu^{(2)} \geq 0$ constant material parameters, $\{\lambda_1^2, \lambda_2^2, \lambda_3^2\}$ denote the eigenvalues of $\mathbf{FF}^T$, with $\mathbf{F}$ the deformation gradient from the reference cross-linking state, satisfying $\det \mathbf{F} = 1$, and $\{\alpha_1^2, \alpha_2^2, \alpha_3^2\}$ represent the eigenvalues of $\mathbf{AA}^T$, with $\mathbf{A} = \mathbf{G}^{-1}\mathbf{FG}_0$ the local elastic deformation tensor satisfying $\det \mathbf{A} = 1$, while $\mathbf{G}_0$ and $\mathbf{G}$ are the natural deformation tensors due to the nematic director in the reference and current configuration, respectively.

Assuming that the LCE is intrinsically uniaxial, the natural deformation tensor takes the form

$$\mathbf{G} = a^{-1/6}\mathbf{I} + \left(a^{1/3} - a^{-1/6}\right)\mathbf{n} \otimes \mathbf{n},$$ (2)

where $\mathbf{n}$ is the local nematic director, $\otimes$ denotes the tensor product of two vectors, $\mathbf{I} = \text{diag}(1, 1, 1)$ is the identity tensor, and

$$a = \frac{1 + 2Q}{1 - Q}$$ (3)

represents the natural shape parameter, with Q the scalar uniaxial order parameter ($Q = 1$ corresponds to perfect nematic order and $Q = 0$ to the case where mesogens are randomly oriented) [9]. For the reference configuration, $\mathbf{G}$ is replaced by $\mathbf{G}_0$, with $\mathbf{n}_0$, a_0 and Q_0 instead of $\mathbf{n}$, a and Q, respectively.

Note that, when $\mu^{(2)} = 0$, the phenomenological model in Eq. 1 reduces to the neo-Hookean model for rubber [47], and when $\mu^{(1)} = 0$, it simplifies to the neoclassical model for LCEs [1, 2].

The nematic elastomer modelled by Eq. 1 is subject to the finite-strain deformation with macroscopic stretch ratios

$$\lambda_1 = \lambda > 1, \qquad \lambda_2 = \lambda_3 = \lambda^{-1/2},$$ (4)

while the tensile force is parallel to the nematic director in the current configuration, so that

$$\mathbf{G} = \text{diag}\left(\left(\frac{1 + 2Q}{1 - Q}\right)^{1/3}, \left(\frac{1 - Q}{1 + 2Q}\right)^{1/6}, \left(\frac{1 - Q}{1 + 2Q}\right)^{1/6}\right).$$ (5)

Taking $\mathbf{G}_0 = \mathbf{I}$, we have

$$\lambda_1 = \alpha_1\left(\frac{1 + 2Q}{1 - Q}\right)^{1/3} = \lambda, \qquad \lambda_2 = \alpha_2\left(\frac{1 - Q}{1 + 2Q}\right)^{1/6}, \qquad \lambda_3 = \alpha_3\left(\frac{1 - Q}{1 + 2Q}\right)^{1/6},$$ (6)

and

$$\alpha_1 = \lambda\left(\frac{1 + 2Q}{1 - Q}\right)^{-1/3} = \alpha, \qquad \alpha_2 = \alpha_3 = \lambda^{-1/2}\left(\frac{1 - Q}{1 + 2Q}\right)^{-1/6} = \alpha^{-1/2}.$$ (7)

For uniaxial tension, the principal components of the first Piola-Kirchhoff stress tensor are, respectively,

$$P_1 = \frac{\partial W^{(lce)}}{\partial \lambda_1} - p\lambda_1^{-1} = P > 0,$$ (8)

$$P_2 = \frac{\partial W^{(lce)}}{\partial \lambda_2} - p\lambda_2^{-1} = 0,$$ (9)

$$P_3 = \frac{\partial W^{(lce)}}{\partial \lambda_3} - p\lambda_3^{-1} = 0,$$ (10)

where p is the Lagrange multiplier for the incompressibility constraint, also known as the *arbitrary hydrostatic pressure* [31].

3 Necking

To study necking, we denote by $w(\lambda)$ the strain-energy function given by Eq. 1 with the stretch ratio λ given in Eq. 4 as the only variable. The first derivative of this function is equal to the applied tensile stress, i.e.,

$$w'(\lambda) = \left(P_1 + p\lambda_1^{-1}\right)\frac{\partial\lambda_1}{\partial\lambda} + p\lambda_2^{-1}\frac{\partial\lambda_2}{\partial\lambda} + p\lambda_3^{-1}\frac{\partial\lambda_3}{\partial\lambda} = P, \tag{11}$$

and necking forms when the applied stress P first increases, then decreases, then increases again as λ increases [31]. It can be shown that, when Q is constant, $w''(\lambda) > 0$, therefore necking cannot occur if Q is independent of deformation. A more general result is proved in Appendix A of this paper.

We let Q depend on the deformation through the following constitutive relation obtained by calibration to experimental data of [14] (see Fig. 3(a) and also Appendix B of this paper):

$$Q = 0.35 \left[\frac{e^{16(\lambda-1.45)} - 1}{e^{16(\lambda-1.45)} + 1} - \frac{e^{16} - 1}{e^{16} + 1} + 2 \right], \qquad \text{for } \lambda \geq 1. \tag{12}$$

It remains to verify numerically that the second derivative $w''(\lambda)$ of $w(\lambda)$ will change sign for some $\lambda \in (1, 2)$. For different values of $\eta = \mu^{(1)}/\mu^{(2)}$, the nondimensionalised function $w(\lambda)$ (i.e., the function divided by $\mu^{(2)}$) and its first two derivatives are plotted in Fig. 3(b)-(d), respectively. These plots suggest that, as η increases, the necking interval (i.e., the interval where $w''(\lambda) < 0$) decreases, and there is a critical value $\eta_{crt} \approx 4.55$ above which necking does not form. For example, when $\eta = 3$,
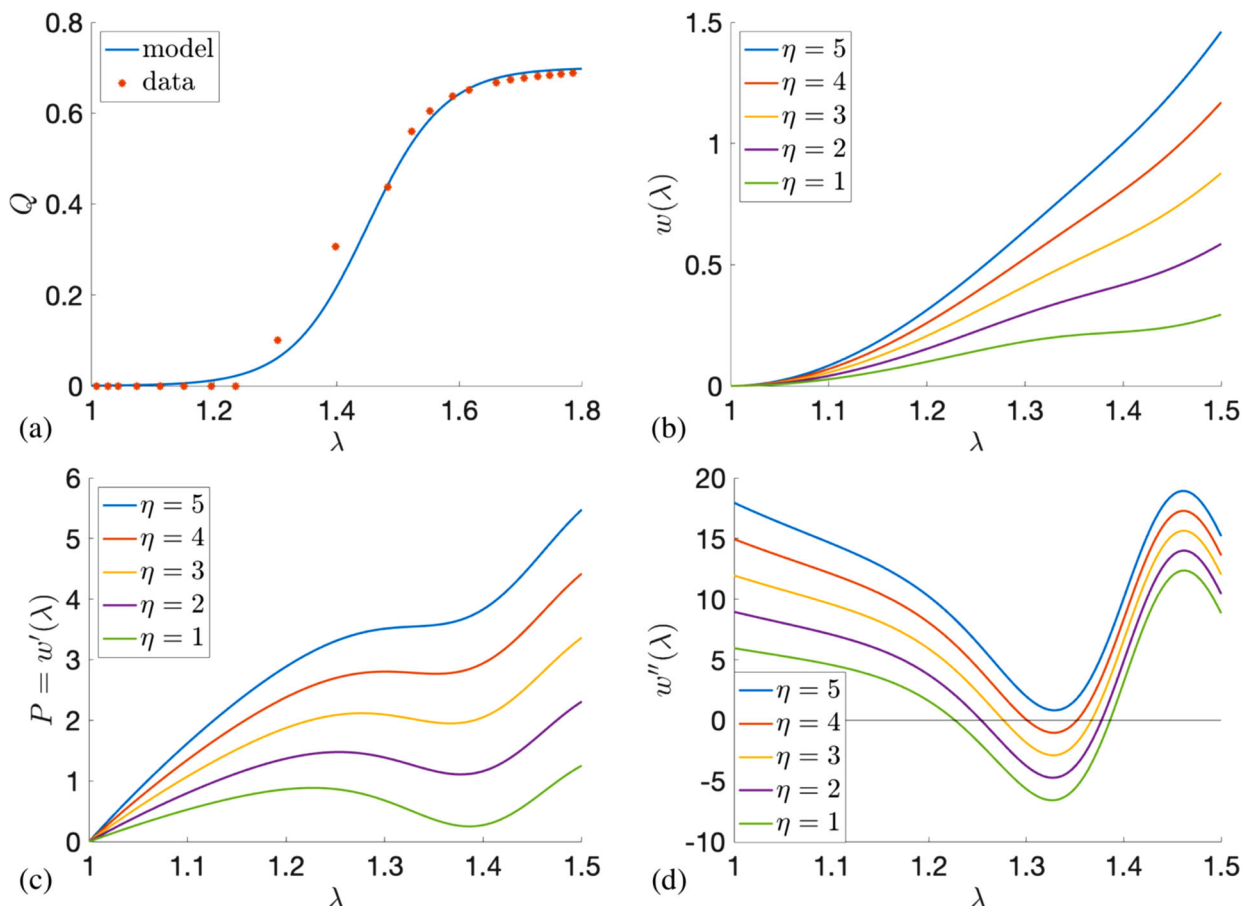

Fig. 3 (a) The uniaxial order parameter Q given by Eq. 12 and the associated experimental data [14]; (b) The nondimensionalised strain-energy function $w(\lambda)$, for different values of $\eta = \mu^{(1)}/\mu^{(2)}$; (c) The applied tensile stress $P = w'(\lambda)$; (d) The second derivative $w''(\lambda)$ of the strain-energy function $w(\lambda)$

$w''(\lambda)$ changes from positive to negative at $\lambda_* \approx 1.28$, then from negative to positive at $\lambda^* \approx 1.37$. In this case, necking occurs for $1.28 < \lambda < 0.37$. When $\eta \to \infty$, the model reduces to the neo-Hookean model for rubber, which does not exhibit necking.

4 Shear striping

Next, we analyse shear striping under uniaxial stress. In this case, we assume that the nematic director only rotates in the biaxial plane while the uniaxial order parameter Q remains constant. This assumption about the order parameter is consistent with experimental observations showing relatively small variations before, during and after stripe formation [21, 23, 46, 52].

In a Cartesian system of coordinates, we define the nematic director in the reference and stretched configuration, respectively, as

$$\mathbf{n}_0 = \begin{bmatrix} 1 \\ 0 \\ 0 \end{bmatrix}, \qquad \mathbf{n} = \begin{bmatrix} \cos\theta \\ \sin\theta \\ 0 \end{bmatrix}, \tag{13}$$

where $\theta \in [0, \pi/2]$ is the angle between $\mathbf{n}$ and $\mathbf{n}_0$. The associated natural deformation tensors take the form, respectively,

$$\mathbf{G}_0 = \begin{bmatrix} a^{1/3} & 0 & 0 \\ 0 & a^{-1/6} & 0 \\ 0 & 0 & a^{-1/6} \end{bmatrix} \tag{14}$$

and

$$\mathbf{G} = \begin{bmatrix} a^{-1/6} + \left(a^{1/3} - a^{-1/6}\right)\cos^2\theta & \left(a^{1/3} - a^{-1/6}\right)\sin\theta\cos\theta & 0 \\ \left(a^{1/3} - a^{-1/6}\right)\sin\theta\cos\theta & a^{-1/6} + \left(a^{1/3} - a^{-1/6}\right)\sin^2\theta & 0 \\ 0 & 0 & a^{-1/6} \end{bmatrix}, \tag{15}$$

where a is defined in terms of Q by Eq. 3, and we emphasise that now Q, and therefore a, is fixed.

It is standard procedure in any analytical study of elastic instabilities to consider small perturbations around an equilibrium deformation of interest [19, 32, 34, 35]. To demonstrate shear striping, we take the following perturbed deformation gradient

$$\mathbf{F} = \begin{bmatrix} \lambda^{-1/2} & 0 & 0 \\ \varepsilon & \lambda & 0 \\ 0 & 0 & \lambda^{-1/2} \end{bmatrix}, \tag{16}$$

where $\lambda > 1$ is the finite stretch ratio in the tensile direction and $0 < \varepsilon \ll 1$ is the small shear perturbation. The corresponding elastic deformation tensor is equal to

$$\mathbf{A} = \begin{bmatrix} \lambda^{-1/2}\left(a^{1/2}\sin^2\theta + \cos^2\theta\right) & \lambda\left(a^{-1/2} - 1\right)\sin\theta\cos\theta & 0 \\ \lambda^{-1/2}\left(1 - a^{1/2}\right)\sin\theta\cos\theta & \lambda\left(a^{-1/2}\sin^2\theta + \cos^2\theta\right) & 0 \\ 0 & 0 & \lambda^{-1/2} \end{bmatrix}$$
$$+ \varepsilon \begin{bmatrix} \left(1 - a^{1/2}\right)\sin\theta\cos\theta & 0 & 0 \\ \left(\sin^2\theta + a^{1/2}\cos^2\theta\right) & 0 & 0 \\ 0 & 0 & 0 \end{bmatrix}. \tag{17}$$

We study these perturbations around two equilibrium solutions where λ is finite and fixed and $(\varepsilon, \theta) = (0, 0)$ or $(\varepsilon, \theta) = (0, \pi/2)$, corresponding to the director being perpendicular (when in the reference state) or parallel (when fully rotated) to the applied tensile force, respectively.

We denote by $w(\lambda, \varepsilon, \theta)$ the strain-energy function described by Eq. 1, depending only on λ, ε and θ, which takes the following form,

$$w(\lambda, \varepsilon, \theta) = \frac{\mu^{(1)}}{2}\left(\lambda^2 + 2\lambda^{-1} + \varepsilon^2 - 3\right)$$
$$+ \frac{\mu^{(2)}}{2}\left\{\left[\lambda^{-1/2}\left(a^{1/2}\sin^2\theta + \cos^2\theta\right) + \varepsilon\left(1 - a^{1/2}\right)\sin\theta\cos\theta\right]^2\right.$$

$$+ \left[\lambda^{-1/2} \left(1 - a^{1/2} \right) \sin \theta \cos \theta + \varepsilon \left(\sin^2 \theta + a^{1/2} \cos^2 \theta \right) \right]^2 \tag{18}$$

$$+ \left[\lambda \left(a^{-1/2} - 1 \right) \sin \theta \cos \theta \right]^2 + \left[\lambda \left(a^{-1/2} \sin^2 \theta + \cos^2 \theta \right) \right]^2 + \lambda^{-1} - 3 \Big\} .$$

When the finite stretch ratio λ is specified, the equilibrium solution satisfies the following simultaneous equations for energy minimisation,

$$\frac{\partial w(\lambda, \varepsilon, \theta)}{\partial \varepsilon} = 0 \quad \text{and} \quad \frac{\partial w(\lambda, \varepsilon, \theta)}{\partial \theta} = 0. \tag{19}$$

Differentiating the function described by Eq. 18 with respect to ε and θ, respectively, gives

$$\frac{\partial w(\lambda, \varepsilon, \theta)}{\partial \varepsilon} = \mu^{(1)} \varepsilon + \mu^{(2)} \left\{ \left[\lambda^{-1/2} \left(a^{1/2} \sin^2 \theta + \cos^2 \theta \right) + \varepsilon \left(1 - a^{1/2} \right) \sin \theta \cos \theta \right] \left(1 - a^{1/2} \right) \sin \theta \cos \theta \right.$$
$$\left. + \left[\lambda^{-1/2} \left(1 - a^{1/2} \right) \sin \theta \cos \theta + \varepsilon \left(\sin^2 \theta + a^{1/2} \cos^2 \theta \right) \right] \left(\sin^2 \theta + a^{1/2} \cos^2 \theta \right) \right\} \tag{20}$$

and

$$\frac{\partial w(\lambda, \varepsilon, \theta)}{\partial \theta} = \mu^{(2)} \left\{ \left(a^{1/2} - 1 \right) \left[2\lambda^{-1/2} \sin \theta \cos \theta + \varepsilon \left(\sin^2 \theta - \cos^2 \theta \right) \right] \right.$$
$$\cdot \left[\lambda^{-1/2} \left(a^{1/2} \sin^2 \theta + \cos^2 \theta \right) + \varepsilon \left(1 - a^{1/2} \right) \sin \theta \cos \theta \right]$$
$$+ \left(a^{1/2} - 1 \right) \left[\lambda^{-1/2} \left(\sin^2 \theta - \cos^2 \theta \right) - 2\varepsilon \sin \theta \cos \theta \right] \tag{21}$$
$$\cdot \left[\lambda^{-1/2} \left(1 - a^{1/2} \right) \sin \theta \cos \theta + \varepsilon \left(\sin^2 \theta + a^{1/2} \cos^2 \theta \right) \right]$$
$$+ \lambda^2 \left(a^{-1} - 1 \right) \sin \theta \cos \theta \Big\} .$$

At $\varepsilon = 0$ and $\theta = 0$, the partial derivatives defined by Eqs. 20-21 are equal to zero, i.e., this solution is always an equilibrium state. For sufficiently small values of ε and θ, we can write the second order approximation

$$w(\lambda, \varepsilon, \theta) \approx w(\lambda, 0, 0) + \frac{1}{2} \left(\varepsilon^2 \frac{\partial^2 w}{\partial \varepsilon^2}(\lambda, 0, 0) + 2\varepsilon\theta \frac{\partial^2 w}{\partial \varepsilon \partial \theta}(\lambda, 0, 0) + \theta^2 \frac{\partial^2 w}{\partial \theta^2}(\lambda, 0, 0) \right), \tag{22}$$

where

$$\frac{\partial^2 w}{\partial \varepsilon^2}(\lambda, 0, 0) = \mu^{(1)} + \mu^{(2)} a, \tag{23}$$

$$\frac{\partial^2 w}{\partial \varepsilon \partial \theta}(\lambda, 0, 0) = \mu^{(2)} \lambda^{-1/2} \left(1 - a \right), \tag{24}$$

$$\frac{\partial^2 w}{\partial \theta^2}(\lambda, 0, 0) = \mu^{(2)} \left(\lambda^2 - \lambda^{-1} a \right) \left(a^{-1} - 1 \right). \tag{25}$$

First, we find the equilibrium value θ_0 for θ as a function of ε by solving the second equation in Eq. 19. By the approximation (22), the corresponding equation takes the form

$$\varepsilon \frac{\partial^2 w}{\partial \varepsilon \partial \theta}(\lambda, 0, 0) + \theta \frac{\partial^2 w}{\partial \theta^2}(\lambda, 0, 0) = 0, \tag{26}$$

implying

$$\theta_0(\varepsilon) = -\varepsilon \frac{\partial^2 w}{\partial \varepsilon \partial \theta}(\lambda, 0, 0) / \frac{\partial^2 w}{\partial \theta^2}(\lambda, 0, 0). \tag{27}$$

Next, substituting $\theta = \theta_0(\varepsilon)$ in Eq. 22 yields the following function in ε,

$$w(\lambda, \varepsilon, \theta_0(\varepsilon)) - w(\lambda, 0, 0) \approx \frac{\varepsilon^2}{2} \left[\frac{\partial^2 w}{\partial \varepsilon^2}(\lambda, 0, 0) - \left(\frac{\partial^2 w}{\partial \varepsilon \partial \theta}(\lambda, 0, 0) \right)^2 / \frac{\partial^2 w}{\partial \theta^2}(\lambda, 0, 0) \right]. \tag{28}$$

Depending on whether the expression on the right-hand side is negative, zero, or positive, the respective equilibrium state is unstable, neutrally stable, or stable. We deduce that the equilibrium state with $\varepsilon = 0$ and $\theta = 0$ is unstable if

$$a^{1/3} \left(\frac{\eta + 1}{\eta + a} \right)^{1/3} < \lambda < a^{1/3}, \tag{29}$$

where $\eta = \mu^{(1)} / \mu^{(2)}$.

Similarly, at $\varepsilon = 0$ and $\theta = \pi/2$, both the partial derivatives defined by Eqs. 20-21 are equal to zero, and

$$\frac{\partial^2 w}{\partial \varepsilon^2} (\lambda, 0, \pi/2) = \mu^{(1)} + \mu^{(2)}, \tag{30}$$

$$\frac{\partial^2 w}{\partial \varepsilon \partial \theta} (\lambda, 0, \pi/2) = \mu^{(2)} \lambda^{-1/2} (a - 1), \tag{31}$$

$$\frac{\partial^2 w}{\partial \theta^2} (\lambda, 0, \pi/2) = \mu^{(2)} \left(\lambda^2 - \lambda^{-1} a \right) \left(1 - a^{-1} \right). \tag{32}$$

Thus the equilibrium state with $\varepsilon = 0$ and $\theta = \pi/2$ is unstable if

$$a^{1/3} < \lambda < a^{1/3} \left(\frac{\eta + a}{\eta + 1} \right)^{1/3}. \tag{33}$$

Therefore, shear stripes can form when λ satisfies (see also partial results in the Appendix of [32])

$$a^{1/3} \left(\frac{\eta + 1}{\eta + a} \right)^{1/3} < \lambda < a^{1/3} \left(\frac{\eta + a}{\eta + 1} \right)^{1/3}. \tag{34}$$

For the corresponding equilibrium solution, the shear parameter and director angle take the following explicit form, respectively:

$$\varepsilon_0 = \pm \frac{\sqrt{\left[\lambda^3 (\eta + a) - a (\eta + 1) \right] \left[a (\eta + a) - \lambda^3 (\eta + 1) \right]}}{a \lambda^{1/2} (2\eta + a + 1)}, \tag{35}$$

$$\theta_0 = \pm \arctan \sqrt{\frac{\lambda^3 (\eta + a) - a (\eta + 1)}{a (\eta + a) - \lambda^3 (\eta + 1)}}. \tag{36}$$

The gradient tensors for alternating shear deformations in two adjacent stripe subdomains are $\mathbf{F}_\pm$ with $\varepsilon = \pm \varepsilon_0$, respectively. These two deformations are geometrically compatible in the sense that $\mathbf{F}_+$ and $\mathbf{F}_-$ are rank-one connected, i.e., rank $(\mathbf{F}_+ - \mathbf{F}_-) = 1$ [36].

The nondimensionalised strain-energy function $w(\lambda, \varepsilon, \theta)$ (i.e., the function divided by $\mu^{(2)}$) described by Eq. 18, with $\eta = \mu^{(1)} / \mu^{(2)} = 1$, is illustrated in Fig. 4. For λ with values between the lower and upper bounds given by Eq. 34, the minimum energy is attained for $(\varepsilon, \theta) = (\varepsilon_0, \theta_0)$ provided by Eqs. 35-36. Figure 5 depicts the positive values of the shear parameter ε_0 and director angle θ_0 described by Eqs. 35 and 36, respectively, for different parameter ratios η. When $\eta = 0$, corresponding to the neoclassical form, shear stripes form for $\lambda \in \left(1, a^{2/3} \right)$. When $\eta \to \infty$, there is no shear striping since the material is practically purely elastic.

4.1 Optimal stripe width

For shear striping, the width of each subdomain depends on the material properties, sample geometry and boundary conditions. Dirichlet conditions fixing the director at both ends of the LCE sample in its initial orientation, i.e., perpendicular to the

Fig. 4 The nondimensionalised strain-energy function $w(\lambda, \varepsilon, \theta)$ given by Eq. 18, for $(\varepsilon, \theta) = (0, 0)$, $(\varepsilon, \theta) = (\varepsilon_0, \theta_0)$, and $(\varepsilon, \theta) = (0, \pi/2)$, when $a = 4$ and $\eta = 1$ (i.e., $\mu^{(1)} = \mu^{(2)}$). The two vertical lines correspond to the lower and upper bounds on λ. Between these bounds, the second solution, with $(\varepsilon, \theta) = (\varepsilon_0, \theta_0)$, minimises the energy
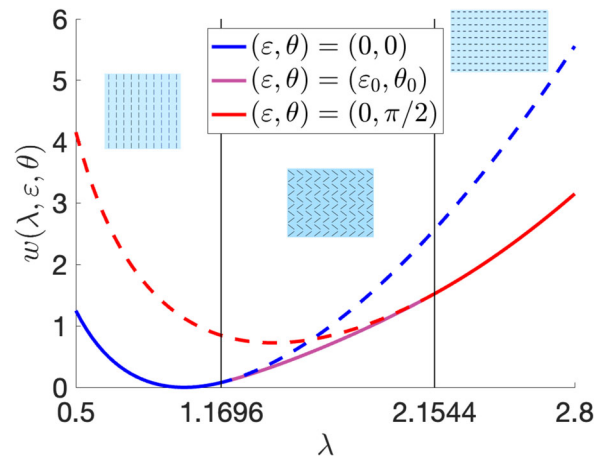
longitudinal direction, known as *strong anchoring*, play an important role in numerically capturing this property. To estimate the stripe width, we add the Frank energy density to our model function, as follows,

$$W^{(nlce)} = W^{(lce)} + \frac{\mathrm{k}}{2} \left| \mathbf{F}^T \operatorname{Grad} \mathbf{n} \right|^2, \tag{37}$$

where $W^{(lce)}$ is as defined in Eq. 1 and k is the Frank constant [9, 49].

We denote by L_1, L_2, L_3 the size of the undeformed LCE sample in the extension direction (which is perpendicular to the director orientation in the undeformed state), the width direction (which is parallel to the initial director), and the thickness direction, respectively. Provided that Dirichlet boundary conditions are imposed at the ends, the width h of a strip band forming parallel to the initial director at each of these ends must be of the same order of magnitude as that of a shear stripe [48] (see also [49, Appendix C]). For geometric compatibility, the displacement in such a strip band must be equal to γh, where $\gamma = \lambda_{12}(x_1, x_2)$ denotes the shear strain in a shear stripe, so that

$$\frac{\mathrm{d}\lambda_{12}}{\mathrm{d}x_2} = \frac{\mathrm{d}\lambda_{22}}{\mathrm{d}x_1}, \tag{38}$$

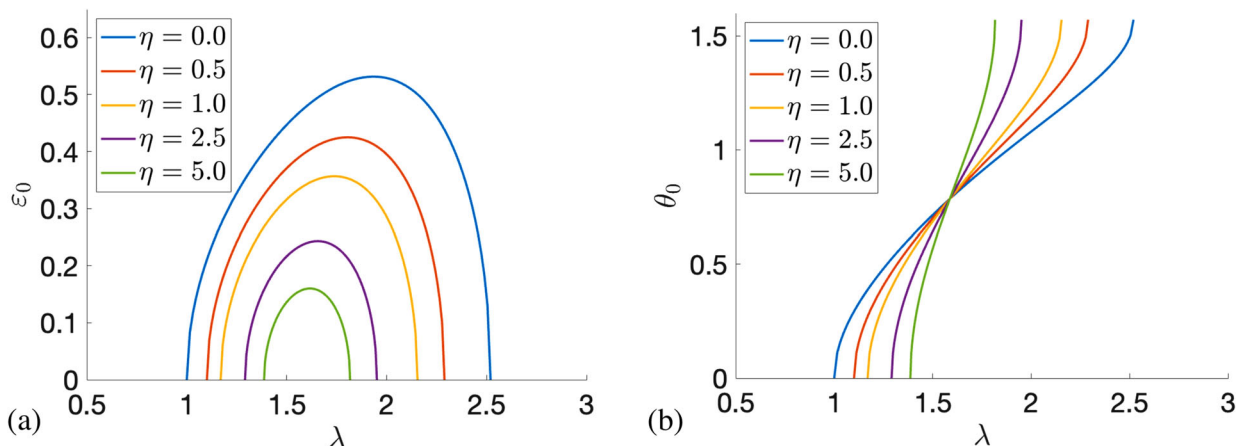with $\lambda_{22} \approx h$ representing the stretch ratio in the direction of the stripe width.

Fig. 5 The positive values of the (a) shear parameter ε_0 and (b) director angle θ_0 given by Eqs. 35-36, for different values of the parameter ratio $\eta = \mu^{(1)}/\mu^{(2)}$ when $a = 4$

Due to the infinitesimal scale of the strip band width, the linear elastic framework is suitable to analyse their deformation. The corresponding elastic energy is then approximately

$$E_{end} \approx \frac{1}{2}\mu\gamma^2\left(2L_3h^2\right)\frac{L_2}{h} = \mu\gamma^2 L_2 L_3 h, \tag{39}$$

where $L_3 h^2$ is the volume of one end region for a single shear stripe and L_2/h is the number of stripes. This elastic energy decreases as h decreases.

There is additional elastic energy at the narrow interface between adjacent stripes with opposite shear deformation and director rotation. Since the director angle $\theta \in (-\theta_0, \theta_0)$ varies from one side of the interface to the other, so that it takes the value zero in the middle of the interval, this energy is approximately

$$E_{int} \approx L_1 L_3 \sqrt{\mu k}\left(\frac{L_2}{h} - 1\right), \tag{40}$$

where $\sqrt{\mu k}$ is the effective surface tension, $L_1 L_3$ is the area of a single interface, and $L_2/h - 1$ is the number of interfaces. This energy tends to decrease when h increases.

The problem is then to find the optimal stripe width h that minimises the total energy

$$E_{stripe} = E_{end} + E_{int}. \tag{41}$$

Differentiating the above function with respect to h and solving for the critical value, we obtain

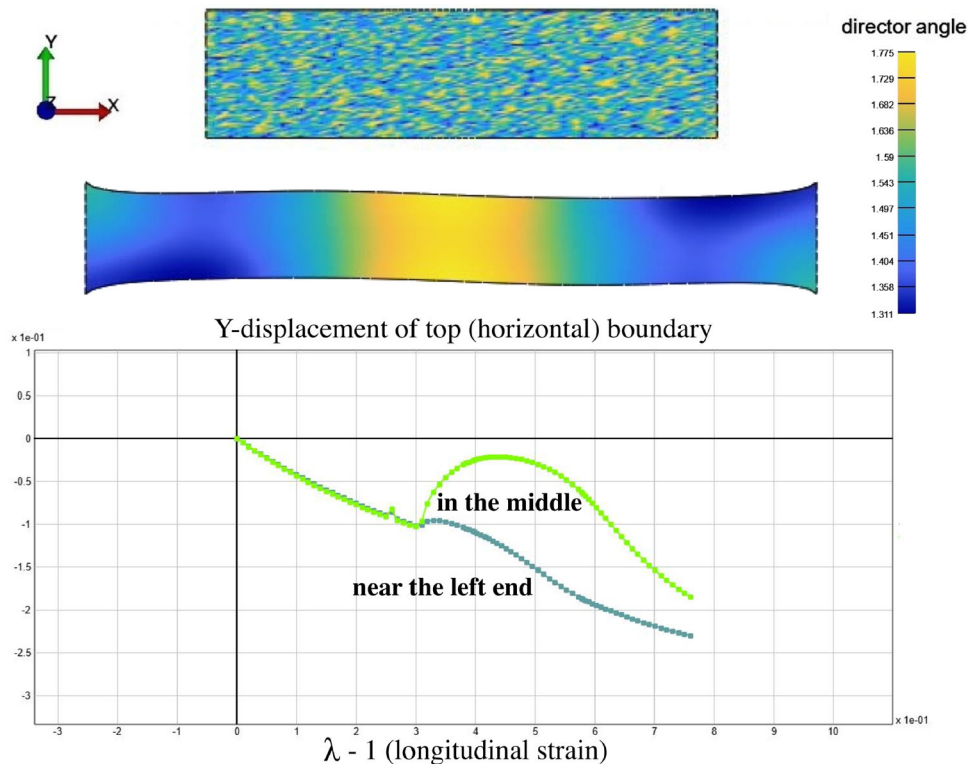$$h \approx \left(L\sqrt{\frac{k}{\mu}}\right)^{1/2}, \tag{42}$$

Fig. 6 Finite element simulation of necking in a nematic LCE described by Eq. 1 when $\eta = \mu^{(1)}/\mu^{(2)} = 3$. Top image shows the reference configuration, middle image shows the deformed state with the director orientation, and bottom plot is for the vertical displacement in the middle and near the left end of the top horizontal boundary

i.e., the stripe width increases with sample initial length $L_1 = L$ and nematic penetration depth $\sqrt{k/\mu} \approx 10^{-8}$ m, which measures the competition between polymer and Frank elasticity. A typical value for the stripe width is $h \approx 10^{-5}$ m.

5 Numerical simulations

We illustrate numerically the stretch deformation causing necking and the periodic shear striping for nematic LCEs.

For the computed examples, we build on existing procedures for three-dimensional finite elasticity of the open-source software Finite Elements for Biomechanics (FEBio) [29], to account also for macroscopic nematic effects in continuum LCE models [28]. Under uniaxial stretch [49], we impose Dirichlet boundary conditions on each side parallel to the Y-directions, where the displacement in all directions is prescribed and the nematic director is fixed, and treat all the other boundaries as free.

Figure 6 presents a finite element simulation of necking where the model function is given by Eq. 1 with $3\mu^{(1)} = \mu^{(2)} = 10^4$ Pa. In this figure, the deformed configuration appears narrower near the ends than in the middle. This is confirmed by the plots showing the corresponding vertical displacements as stretching increases. The darker colour at the ends of the deformed state further suggest that the director is less aligned with the tensile direction compared to the middle section.

Figures 7-8 show finite element representations of shear striping in a nematic LCE described by Eq. 37 with $\mu^{(1)} = \mu^{(2)} = 5 \cdot 10^4$ Pa and $k = 10^{-11}$ N. In Fig. 7, for two samples with different aspect ratios, the number of stripes reduces almost by half when the initial length L increases 4 times. In Fig. 8, the number of stripes reduces by ≈ 3 when Frank constant k increases 100 times, and by ≈ 5 when this constant increases 1,000 times. This is in agreement with our Eq. 42.

Our numerical implementations are openly available at the web address indicated in the data statement of this paper.
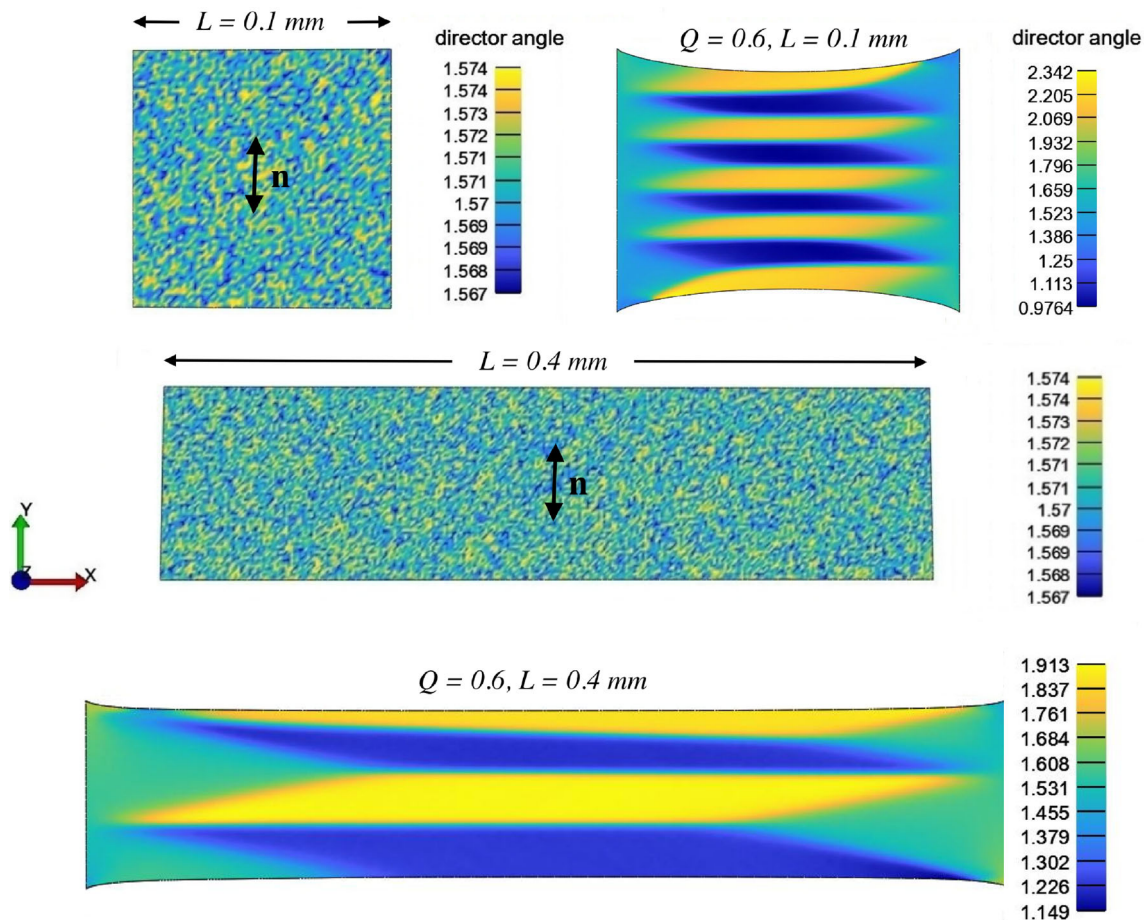

Fig. 7 Finite element simulation of nematic LCEs described by Eq. 37, with $\eta = \mu^{(1)}/\mu^{(2)} = 1$, where stripe width increases with the sample initial length L. Both the reference and deformed configurations are shown
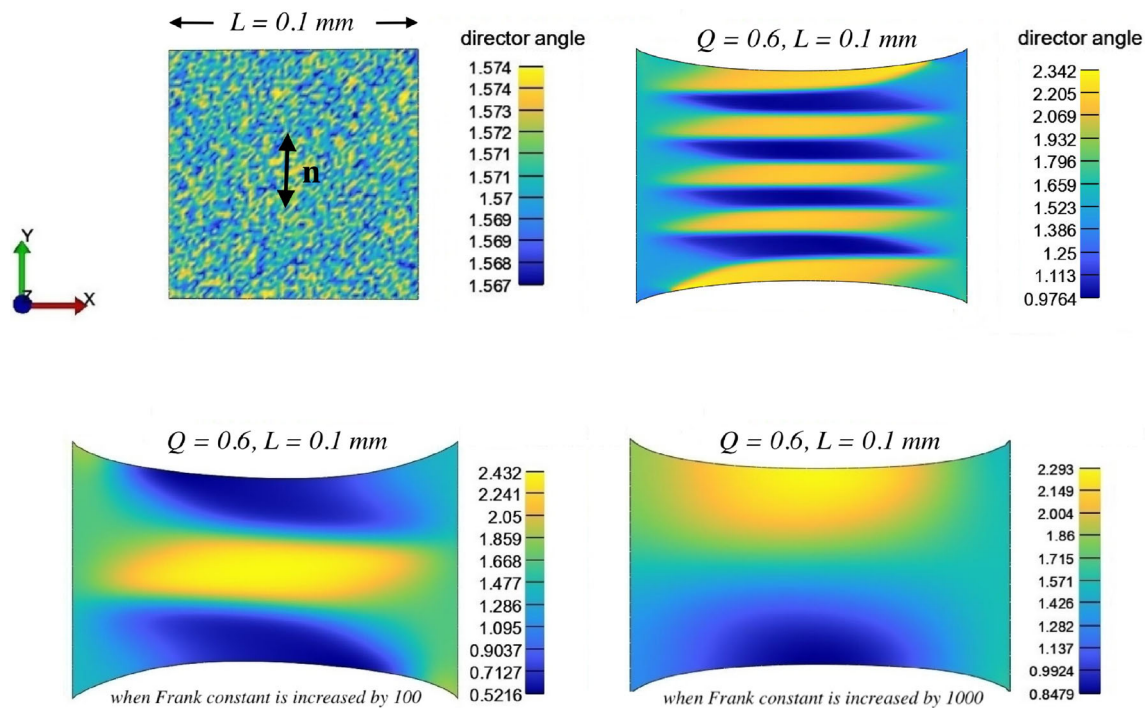
Fig. 8 Finite element simulation of nematic LCEs described by Eq. 37, with $\eta = \mu^{(1)}/\mu^{(2)} = 1$, where stripe width increases with the nematic penetration depth $\sqrt{\kappa/\mu}$ ($\mu = \mu^{(1)} + \mu^{(2)}$). Both the reference and deformed configurations are shown

6 Conclusion

We have demonstrate theoretically and numerically deformation localisation through necking and shear striping in nematic elastomer models. These two instability mechanisms appear in certain nematics LCEs when subject to uniaxial tensile stress. For necking, the scalar uniaxial order parameter varies, reflecting the polydomain-monodomain transition under mechanical stretch. For shear striping, the order parameter is fixed, as reported by experimental studies. Our finite element simulations capture well both of these phenomena. The modelling approaches adopted here can further be extended to include probabilistic model parameters [31] and strain rate effects [4, 51].

A   Nematic elastomer models where necking cannot form

In this appendix, we consider the following strain-energy functions describing a nematic LCE,

$$W^{(nc)}(\mathbf{F}, \mathbf{n}) = W(\mathbf{A}), \tag{A.1}$$

where $\mathbf{F}$ represents the macroscopic deformation gradient from the cross-linking state, $\mathbf{n}$ is the nematic director in the present configuration, and $W(\mathbf{A})$ is the strain-energy density of the isotropic polymer network, depending only on the (local) elastic deformation tensor $\mathbf{A} = \mathbf{G}^{-1}\mathbf{F}\mathbf{G}_0$, with $\mathbf{G}_0$ and $\mathbf{G}$ the natural deformation tensors due to the liquid crystal director in the reference and current configuration, respectively.

The LCE is subject to the finite-strain deformation with $\lambda_1 = \lambda > 1$ and $\lambda_2 = \lambda_3 = \lambda^{-1/2}$, while the tensile force is parallel to the nematic director. Let $\mathbf{G}_0 = \mathbf{I}$, so that

$$\alpha_1 = \lambda \left(\frac{1+2Q}{1-Q}\right)^{-1/3} = \alpha, \qquad \alpha_2 = \alpha_3 = \lambda^{-1/2}\left(\frac{1-Q}{1+2Q}\right)^{-1/6} = \alpha^{-1/2}, \tag{A.2}$$

where $Q \in (0, 1)$ is the scalar uniaxial order parameter in the current configuration.

For hyperelastic materials where the force-extension curve does not have a maximum, the homogeneous deformation is the only absolute minimiser of the elastic energy, hence necking cannot occur [44]. Here, we show that, if Q is constant and the hyperelastic model described by $W(\mathbf{A})$ does not exhibit necking, then the LCE model $W^{(nc)}(\mathbf{F})$ does not present necking either.

To prove this, we denote by $w(\lambda)$ the strain-energy function $W^{(nc)}(\mathbf{F})$ given by Eq. A.1, depending only on λ, and by $\widetilde{w}(\alpha)$ the strain-energy function $W(\mathbf{A})$ for the underlying polymeric network, depending only on α. Calculating the first and second derivatives, we obtain

$$\frac{\mathrm{d}w(\lambda)}{\mathrm{d}\lambda} = \frac{\mathrm{d}\widetilde{w}(\alpha)}{\mathrm{d}\alpha}\frac{\mathrm{d}\alpha}{\mathrm{d}\lambda} = \frac{\mathrm{d}\widetilde{w}(\alpha)}{\mathrm{d}\alpha}\left(\frac{1+2Q}{1-Q}\right)^{-1/3} \tag{A.3}$$

and

$$\frac{\mathrm{d}^2 w(\lambda)}{\mathrm{d}\lambda^2} = \frac{\mathrm{d}^2\widetilde{w}(\alpha)}{\mathrm{d}\alpha^2}\frac{\mathrm{d}\alpha}{\mathrm{d}\lambda}\left(\frac{1+2Q}{1-Q}\right)^{-1/3} = \frac{\mathrm{d}^2\widetilde{w}(\alpha)}{\mathrm{d}\alpha^2}\left(\frac{1+2Q}{1-Q}\right)^{-2/3} > 0. \tag{A.4}$$

The last inequality holds since, by assumption, there is no necking for the polymeric network, hence $\mathrm{d}^2\widetilde{w}/\mathrm{d}\alpha^2 > 0$. It follows that $\mathrm{d}^2 w/\mathrm{d}\lambda^2 > 0$, i.e., for the LCE described by Eq. A.1, necking will not form.

In particular, since incompressible neo-Hookean [47] and Mooney-Rivlin [39, 42] hyperelastic models do not exhibit necking, this property is inherited by the associated LCE models of the form given by Eq. A.1 (see also [35] for alternative modelling).

B   Experimental data

We present in this appendix the experimental data for scalar uniaxial order parameter used to calibrate the function given in Eq. 12 (see also [33]). These data are plotted in Fig. 3(a).

Table 1 Experimental data [14]

λ longitudinal stretch	Q uniaxial order parameter
1.7853	0.6881
1.7658	0.6860
1.7476	0.6838
1.7281	0.6808
1.7061	0.6772
1.6840	0.6727
1.6606	0.6669
1.6164	0.6514
1.5891	0.6365
1.5526	0.6050
1.5227	0.5595
1.4836	0.4378
1.3989	0.3059
1.3037	0.1000
1.2359	0
1.1955	0
1.1512	0
1.1121	0
1.0743	0
1.0443	0
1.0274	0
1.0091	0

Declarations

Conflict of interest The authors have no competing interests to declare that are relevant to the content of this article.

References

1. Bladon, P., Terentjev, E.M., Warner, M.: Transitions and instabilities in liquid crystal elastomers. Phys. Rev. E: Rapid Commun. **47**(6), 3838–3840 (1993). https://doi.org/10.1103/PhysRevE.47.R3838
2. Bladon, P., Terentjev, E.M., Warner, M.: Deformation-induced orientational transitions in liquid crystal elastomers. Journal de Physique II **4**, 75–91 (1994). https://doi.org/10.1051/jp2:1994100
3. Carlson, D.E., Fried, E., Sellers, S.: Force-free states, relative strain, and soft elasticity in nematic elastomers. J. Elasticity **69**, 161–180 (2002). https://doi.org/10.1023/A:1027377904576
4. Chehade, A.E.H., Shen, B., Yakacki, A.M., Nguyen, T.D., Govindjee, S.: Finite element modeling of viscoelastic liquid crystal elastomers. Int. J. Numer. Method Eng. (2024). https://doi.org/10.1002/nme.7510
5. Clarke, S.M., Terentjev, E.M.: Slow stress relaxation in randomly disordered nematic elastomers and gels. Phys. Rev. Lett. **81**(20), 4436–4439 (1998). https://doi.org/10.1103/PhysRevLett.81.4436
6. Clarke, S.M., Terentjev, E.M., Kundler, I., Finkelmann, H.: Texture evolution during the polydomain-monodomain transition in nematic elastomers. Macromolecules **31**(15), 4862–4872 (1998). https://doi.org/10.1021/ma980195j
7. Conti, S., DeSimone, A., Dolzmann, G.: Soft elastic response of stretched sheets of nematic elastomers: a numerical study. J. Mech. Phys. Solids **50**, 1431–1451 (2002). https://doi.org/10.1016/S0022-5096(01)00120-X
8. de Gennes, P.G., Hébert, M., Kant, R.: Artificial muscles based on nematic gels. Macromolecular Symposia **113**, 39–49 (1997). https://doi.org/10.1002/masy.19971130107
9. de Gennes, P.G., Prost, J.: The Physics of Liquid Crystals, 2nd edn. Clarendon Press, Oxford (1993)
10. DeSimone, A., Dolzmann, G.: Material instabilities in nematic elastomers. Physica D **136**(1–2), 175–191 (2000). (doi: S0167-2789(99)00153-0)
11. DeSimone, A., Teresi, L.: Elastic energies for nematic elastomers. European Phys. J. E **29**, 191–204 (2009). https://doi.org/10.1140/epje/i2009-10467-9
12. Ebralidze, T.D.: Weigert hologram. Appl. Opt. **34**(8), 1357–1362 (1995). https://doi.org/10.1364/AO.34.001357
13. Finkelmann, H., Kundler, I., Terentjev, E.M., Warner, M.: Critical stripe-domain instability of nematic elastomers. Journal de Physique II **7**, 1059–1069 (1997). https://doi.org/10.1051/jp2:1997171
14. Fridrikh, S.V., Terentjev, E.M.: Polydomain-monodomain transition in nematic elastomers. Phys. Rev. E **60**, 1847–1857 (1999). https://doi.org/10.1103/PhysRevE.60.1847
15. Fried, E., Sellers, S.: Free-energy density functions for nematic elastomers. J Mech. Phys. Solids **52**(7), 1671–1689 (2004). https://doi.org/10.1016/j.jmps.2003.12.005
16. Fried, E., Sellers, S.: Orientational order and finite strain in nematic elastomers. J. Chem. Phys. **123**(4), 043521 (2005). https://doi.org/10.1063/1.1979479
17. Fried, E., Sellers, S.: Soft elasticity is not necessary for striping in nematic elastomers. J. Appl. Phys. **100**, 043521 (2006). https://doi.org/10.1063/1.2234824
18. Golubović, L., Lubensky, T.C.: Nonlinear elasticity of amorphous solids. Phys. Rev. Lett. **63**, 1082–1085 (1989). https://doi.org/10.1103/PhysRevLett.63.1082
19. Goriely, A., Mihai, L.A.: Liquid crystal elastomers wrinkling. Nonlinearity **34**(8), 5599–5629 (2021). https://doi.org/10.1088/1361-6544/ac09c1
20. He, X., Zheng, Y., He, Q., Cai, S.: Uniaxial tension of a nematic elastomer with inclined mesogens. Extreme Mech. Lett. **40**, 100936 (2020). https://doi.org/10.1016/j.eml.2020.100936
21. Higaki, H., Takigawa, T., Urayama, K.: Nonuniform and uniform deformations of stretched nematic elastomers. Macromolecules **46**, 5223–5231 (2013). https://doi.org/10.1021/ma400771z
22. Kim, J.H., Lee, S.E., Kim, B.H.: Applications of flexible and stretchable three-dimensional structures for soft electronics. Soft Sci. **3**, 16 (2023). https://doi.org/10.20517/ss.2023.07
23. Kundler, I., Finkelmann, H.: Strain-induced director reorientation in nematic liquid single crystal elastomers. Macromolecular Rapid Commun. **16**, 679–686 (1995). https://doi.org/10.1002/marc.1995.030160908

24. Kundler, I., Finkelmann, H.: Director reorientation via stripe-domains in nematic elastomers: influence of cross-link density, anisotropy of the network and smectic clusters. Macromolecular Chemistry and Physics **199**(4), 677–686 (1998). https://doi.org/10.1002/(SICI)1521-3935(19980401)199:4$<$677::AID-MACP677$>$3.0.CO;2-E

25. Küpfer, J., Finkelmann, H.: Nematic liquid single crystal elastomers. Die Makromolekulare Chemie, Rapid Communications **12**, 717–726 (1991). https://doi.org/10.1002/marc.1991.030121211

26. Küpfer, J., Finkelmann, H.: Liquid crystal elastomers: Influence of the orientational distribution of the crosslinks on the phase behaviour and reorientation processes. Macromol. Chem. Phys. **195**, 1353–1367 (1994). https://doi.org/10.1002/macp.1994.021950419

27. Li, M., Yan, Y., Xu, S., Wang, G., Wu, J., Feng, X.Q.: Surface effect on the necking of hyperelastic materials. Current Appl. Phys. **38**, 91–98 (2022). https://doi.org/10.1016/j.cap.2022.03.010

28. Luo, C., Calderer, M.C.: Numerical study of liquid crystal elastomers by a mixed finite element method. European J Appl. Math. **23**, 121–154 (2012). https://doi.org/10.1017/S0956792511000313

29. Maas, S.A., Ellis, B.J., Ateshian, G.A., Weiss, J.: FEBio: Finite Elements for Biomechanics. J. Biomech. Eng. **134134**(1), 011005 (2012). https://doi.org/10.1115/1.4005694

30. Mbanga, B.L., Ye, F., Selinger, J.V., Selinger, R.L.: Modeling elastic instabilities in nematic elastomers. Phys. Rev. E **82**(5), 051701 (2010). https://doi.org/10.1103/PhysRevE.82.051701

31. Mihai, L.A.: Stochastic Elasticity: A Nondeterministic Approach to the Nonlinear Field Theory. Springer Cham, Switzerland (2022). https://doi.org/10.1007/978-3-031-06692-4

32. Mihai, L.A.: A theoretical model for power generation via liquid crystal elastomers. Math. Mech. Solids **29**(6), 1198–1215 (2023). https://doi.org/10.1177/10812865231193735

33. Mihai, L.A., Gablier, A., Terentjev, E.M., Goriely, A.: Anti-Hertz bulging of actuated liquid crystal elastomers. Extreme Mech. Lett. **64**, 102066 (2023). https://doi.org/10.1016/j.eml.2023.102066

34. Mihai, L.A., Goriely, A.: Likely striping in stochastic nematic elastomers. Math. Mech. Solids **25**(10), 1851–1872 (2020). https://doi.org/10.1177/1081286520914958

35. Mihai, L.A., Goriely, A.: Instabilities in liquid crystal elastomers. Material Research Society (MRS) Bulletin **46** (2021). https://doi.org/10.1557/s43577-021-00115-2

36. Mihai, L.A., Goriely, A.: Controllable deformations of unconstrained ideal nematic elastomers. J. Elasticity (2023). https://doi.org/10.1007/s10659-023-10038-5

37. Mihai, L.A., Raistrick, T., Gleeson, H.F., Mistry, D., Goriely, A.: A predictive theoretical model for stretch-induced instabilities in liquid crystal elastomers. Liquid Crystals (2023). https://doi.org/10.1080/02678292.2022.2161655

38. Mitchell, G.R., Davis, F., Guo, W.: Strain-induced transitions in liquid-crystal elastomers. Phys. Rev. Lett. **71**, 2947–2950 (1993). https://doi.org/10.1103/PhysRevLett.71.2947

39. Mooney, M.: A theory of large elastic deformation. J. Appl. Phys. **11**, 582–592 (1940). https://doi.org/10.1063/1.1712836

40. Petelin, A., Čopič, M.: Observation of a soft mode of elastic instability in liquid crystal elastomers. Phys. Rev. Lett. **103**, 077801 (2009). https://doi.org/10.1103/PhysRevLett.103.077801

41. Petelin, A., Čopič, M.: Strain dependence of the nematic fluctuation relaxation in liquid-crystal elastomerss. Phys. Rev. E **82**, 011703 (2010). https://doi.org/10.1103/PhysRevE.82.011703

42. Rivlin, R.S.: Large elastic deformations of isotropic materials. IV. Further developments of the general theory, Philosophical Transactions of the Royal Society of London. Series A, Mathematical and Physical Sciences **241**, 379–397 (1948). https://doi.org/10.1098/rsta.1948.0024

43. Rothemund, P., Kim, Y., Heisser, R.H., Zhao, X., Shepherd, R.F., Keplinger, C.: Shaping the future of robotics through materials innovation. Nature Mater. **20**, 1582–1587 (2021). https://doi.org/10.1038/s41563-021-01158-1

44. Sivaloganathan, J., Spector, S.J.: On the stability of incompressible elastic cylinders in uniaxial extension. J. Elasticity **105**(1–2), 313–330 (2011). https://doi.org/10.1007/s10659-011-9330-9

45. Soltani, M., Raahemifar, K., Nokhosteen, A., Kashkooli, F.M., Zoudani, E.L.: Numerical methods in studies of liquid crystal elastomers. Polymers **13**, 1650 (2021). https://doi.org/10.3390/polym13101650

46. Talroze, R.V., Zubarev, E.R., Kuptsov, S.A., Merekalov, A.S., Yuranova, T.I., Plate, N.A., Finkelmann, H.: Liquid crystal acrylate-based networks: polymer backbone-LC order interaction. Reactive Functional Polymers **41**, 1–11 (1999). https://doi.org/10.1016/S1381-5148(99)00032-2

47. Treloar, L.R.G.: Stress-strain data for vulcanized rubber under various types of deformation. Trans. Faraday Soc. **40**, 59–70 (1944). https://doi.org/10.1039/TF9444000059

48. Verwey, G.C., Warner, M., Terentjev, E.M.: Elastic instability and stripe domains in liquid crystalline elastomers. Journal de Physique II France **6**(9), 1273–1290 (1996). https://doi.org/10.1051/jp2:1996130

49. Warner, M., Terentjev, E.M.: Liquid Crystal Elastomers, paper back. Oxford University Press, Oxford, UK (2007)

50. White, T.J., Broer, D.J.: Programmable and adaptive mechanics with liquid crystal polymer networks and elastomers. Nature Mater. **14**, 1087–1098 (2015). https://doi.org/10.1038/nmat4433

51. Zhang, Y., Xuan, C., Jiang, Y., Huo, Y.: Continuum mechanical modeling of liquid crystal elastomers as dissipative ordered solids. J Mech. Phys. Solids **126**, 285–303 (2019). https://doi.org/10.1016/j.jmps.2019.02.018

52. Zubarev, E.R., Kuptsov, S.A., Yuranova, T.I., Talroze, R.V., Finkelmann, H.: Monodomain liquid crystalline networks: reorientation mechanism from uniform to stripe domains. Liquid Crystals **26**, 1531–1540 (1999). https://doi.org/10.1080/026782999203869

Publisher's Note Springer Nature remains neutral with regard to jurisdictional claims in published maps and institutional affiliations.